Electronic Supplementary Material (ESI) for ChemComm.

Supporting Information

Boosting electrochemical water oxidation through replacement of O_h Co sites in cobalt oxide spinel with manganese

Prashanth W. Menezes,[a] Arindam Indra,[a] Vitaly Gutkin,[b] and Matthias Driess*[a]

[a] *Department of Chemistry, Metalorganics and Inorganic Materials, Technische Universität Berlin, Strasse des 17 Juni 135, D-10623 Berlin, Germany*

[b] *The Harvey M. Krueger Family Center for Nanoscience and Nanotechnology, The Hebrew University of Jerusalem, Edmond J. Safra Campus, Givat Ram, Jerusalem 91904, Israel*

Chemicals

All chemical reagents (analytical grade) were used as received without any further purification. Deionized water was used throughout the experiment. Commercially available cobalt(II) acetate tetrahydrate ($Co(CH_3COO)_2 \cdot 4H_2O$), manganese(II) acetate tetrahydrate ($Mn(CH_3COO)_2 \cdot 4H_2O$) and ammonium oxalate dihydrate ($(NH_4)_2C_2O_4 \cdot 2H_2O$), were obtained from Sigma Aldrich whereas cetyltrimethylammonium bromide (CTAB) was purchased from Alfa Aesar.

Instrumental

Phase identification of the samples were determined using PXRD on a Bruker AXS D8 advanced automatic diffractometer equipped with a position sensitive detector (PSD) and a curved germanium (111) primary monochromator. The radiation used was Cu-*Kα* (λ = 1.5418 Å). The XRD profiles recorded were in the range of $5° < 2\theta < 80°$ and the diffraction pattern fitting were carried out using the program WinxPow. Similarly, the structural models were drawn with the DIAMOND program version 3.0.

The chemical composition of the precursor was confirmed by ICP-AES on a Thermo Jarrell Ash Trace Scan analyzer. The samples were dissolved in acid solutions (aqua regia) and the results of three independent measurements were averaged which showed good agreement with the chemical formulae. The quantification of the precursor and oxide was also estimated by the elemental analyses that were performed on a Flash EA 112 Thermo Finnigan elemental analyzer.

SEM was used to evaluate size and morphology and EDX analyses were used to semi-quantitatively determine the cobalt present on the sample surfaces. The samples were placed on a silicon wafer and the measurements were carried on a LEO DSM 982 microscope integrated with EDX (EDAX, Appollo XPP). Data handling and analysis were carried out with the software package EDAX.

The morphology of the catalysts was investigated by TEM analysis. A small amount of the sample powder was placed on a TEM-grid (carbon film on 300 mesh Cu-grid, Plano GmbH, Wetzlar, Germany). The microstructure (morphology, particle size, phase composition, crystallinity) of the samples was studied by a FEI Tecnai G^2 20 S-TWIN transmission electron microscope (FEI Company, Eindhoven, Netherlands) equipped with a LaB_6-source at 200 kV acceleration voltage. EDX analysis were carried out with an EDAX r-TEM SUTW Detector (Si (Li)-detector). Images were recorded with a GATAN MS794 P CCD-camera. Both SEM and TEM experiments were carried out at the Zentrum für Elektronenmikroskopie (ZELMI) of the TU Berlin.

The surface area and the pore size distributions were conducted on a Quantachrome Autosorb-1 apparatus. Nitrogen adsorption/desorption isotherms were determined at -196 ˚C after degassing the sample at 150 ˚C overnight. The BET surface areas (S_{BET}) were estimated by adsorption data in a relative pressure range from 0.01 to 0.1 and the pore size distribution (PSD) was calculated by analyzing the adsorption data of the N_2 isotherm using the Barret-Joyner-Halenda (BJH) method.

The presence of different modes of vibrations of the precursor and the metal oxides were studied using a BIORAD FTS 6000 FTIR spectrometer under attenuated total reflection (ATR) conditions. The data were recorded in the range of 400–4000 cm^{-1} with the average of thirty two scans at 4 cm^{-1} resolution.

The XPS measurements were carried out using a Kratos Axis Ultra X-ray photoelectron spectrometer (Karatos Analytical Ltd., Manchester, UK) using an Al *Kα* monochromatic radiation source (1486.7 eV) with 90° takeoff angle (normal to analyzer). The vacuum pressure in the analyzing chamber was maintained at 2 x 10^{-9} Torr. The high-resolution XPS spectra were collected for C1*s*, O1*s* and Co2*p* levels with pass energy 20 eV and step 0.1 eV. The binding energies were calibrated relative to C1*s* peak energy position as 285.0 eV. Data analyses were performed using Casa XPS (Casa Software Ltd.) and Vision data processing program (Kratos Analytical Ltd.).

Experimental Section

Synthesis of manganese cobalt oxalate dihydrate, $Mn_xCo_{1-x}C_2O_4{\cdot}2H_2O$ (x = ~ 0.1)

Micro-emulsions containing cetyltrimethylammonium bromide (CTAB, 2.0 g) as a surfactant, 1-hexanol (20 mL) as co-surfactant and hexane (35 mL) as the lipophilic phase were prepared and were mixed separately with an aqueous solution of 0.05 M manganese acetate, 0.05 M cobalt acetate and ammonium oxalate. Each micro-emulsion was mixed slowly and stirred overnight. The pink precipitate then obtained was centrifuged and washed with 1:1 mixture of chloroform and methanol (200 mL) and subsequently dried at 60 ˚C for 12 hours.

Syntheses of manganese cobalt oxides, $Mn_xCo_{3-x}O_4$ (x = ~ 0.3)

The manganese cobalt oxalate precursor was subjected to thermal treatment at 400-550 ˚C in in dry synthetic air (20% O_2, 80% N_2) at 400 ˚C for 8 hours (2 ˚C/min) to obtain the desired mineral phases of manganese cobalt oxide.

Syntheses of manganese oxide, Mn_2O_3 and cobalt oxide, Co_3O_4

The manganese oxalate precursor ($MnC_2O_4 \cdot 2H_2O$) and cobalt oxalate precursor ($CoC_2O_4 \cdot 2H_2O$) were first prepared similar to manganese cobalt precursor which were then subsequently treated thermally in in dry synthetic air to form respective manganese oxide (Mn_2O_3) and cobalt oxide (Co_3O_4)

Electrochemical oxygen evolution reaction (OER) measurements

All electrodes were prepared by electrophoretic deposition with a potential difference of 10 V in a mixture of iodine and acetone on 1x1 cm^2 area of fluorinated tin oxide coated glass (FTO, Sigma Aldrich, resistivity 8-12 Ω/sq.). The loading on each FTO electrode was ~ 1 mg cm^{-2}. Catalytic activity was measured in 0.1 M or 1 M KOH solution at room temperature using single-compartment three-electrode electrochemical cell (catalyst deposited on FTO-glass as working electrode, Pt wire as a counter electrode and Hg/Hg_2SO_4 as a reference electrode) with a potentiostat (SP-200, BioLogic Science Instruments) controlled by EC-Lab v10.20 software package. Cyclic voltammetry was carried out with the typical electrolyte resistance (incl. the electrode) about 40 Ω; *iR* compensation at 80% was applied. The solution was not stirred during the experiments. The potentials reported in this work were referenced to the reversible hydrogen electrode (RHE) through RHE calibration, and in 1 M KOH at pH 14, $E(RHE) = E(Hg/Hg_2SO_4) + 0.82$ V whereas for 0.1 M KOH, $E(RHE) = E(Hg/Hg_2SO_4) + 0.762$ V. Chronoamperometric measurements were performed in 1M KOH at selected constant potentials vs RHE. Nickel foam (NF, Racemat BV) electrodes were also prepared by electrophoretic deposition and the loading on the electrode was ~ 3 mg cm^{-2}. The overall water splitting reaction was performed in a two-electrode system on catalysts deposited on NF.

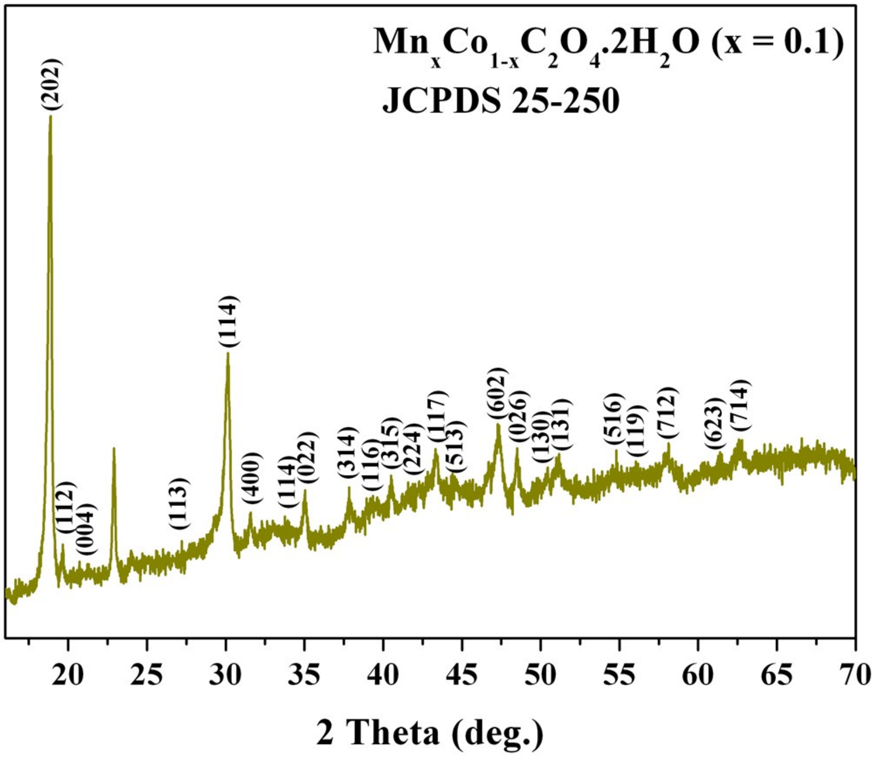

Fig. S1. PXRD and Miller indices (hkl) of as-prepared manganese cobalt oxalate precursor ($Mn_{0.1}Co_{0.9}C_2O_4{\cdot}2H_2O$, JCPDS 25-250) *via* inverse micelle approach. The pattern was slightly shifted in comparison to pure cobalt oxalate dihydrate due to the presence of manganese in the crystal lattice. The amount of manganese and cobalt present in the oxalate was determined by EDX and ICP-AES analysis.

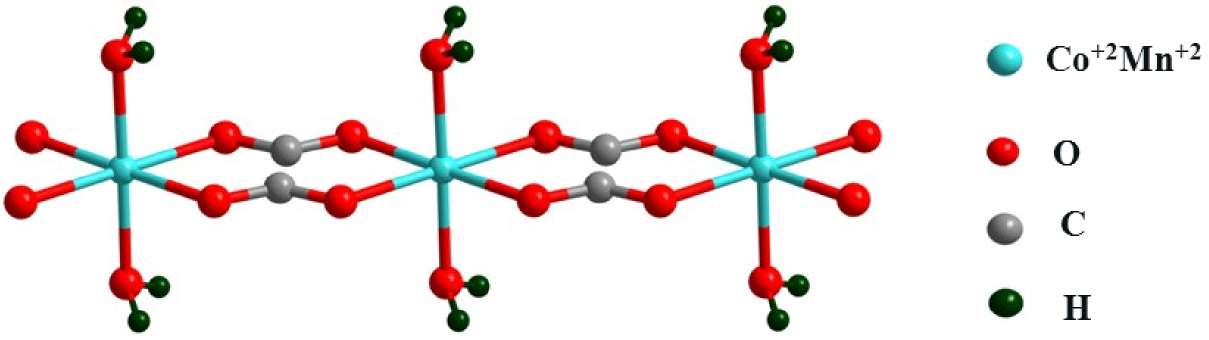

Fig. S2. The crystal structure of manganese cobalt oxalate dihydrate precursor. The crystal structure contains one dimensional chain with each mixed Mn/Co atom coordinated by two bidentate oxalate ligands and two water molecules.[1]

Table S1. Quantification of manganese and cobalt ratio of manganese cobalt oxalate precursor was obtained by EDX and ICP-AES. Three independent measurements were performed for the reliability of the experiments.

	Mn:Co (EDX)	Mn:Co (ICP-AES)
$Mn_xCo_{1-x}C_2O_4{\cdot}2H_2O$ (x = 0.1)	0.10:1	0.10:1
	0.11:1	0.11:1
	0.08:1	0.10:1
Averaged	**0.0970:1**	**0.103:3**

Table S2. Results from the elemental analysis (C, H, N) of as-prepared manganese cobalt oxalate dihydrate that is in accordance with the calculated chemical formula. Three independent measurements were performed to ensure the reliability of the experiments and the averaged value has been presented.

	Carbon (mass%)	Hydrogen (mass%)	Nitrogen (mass%)
Calculated	**13.16**	**2.21**	**0**
Averaged	**13.15**	**2.24**	**0**

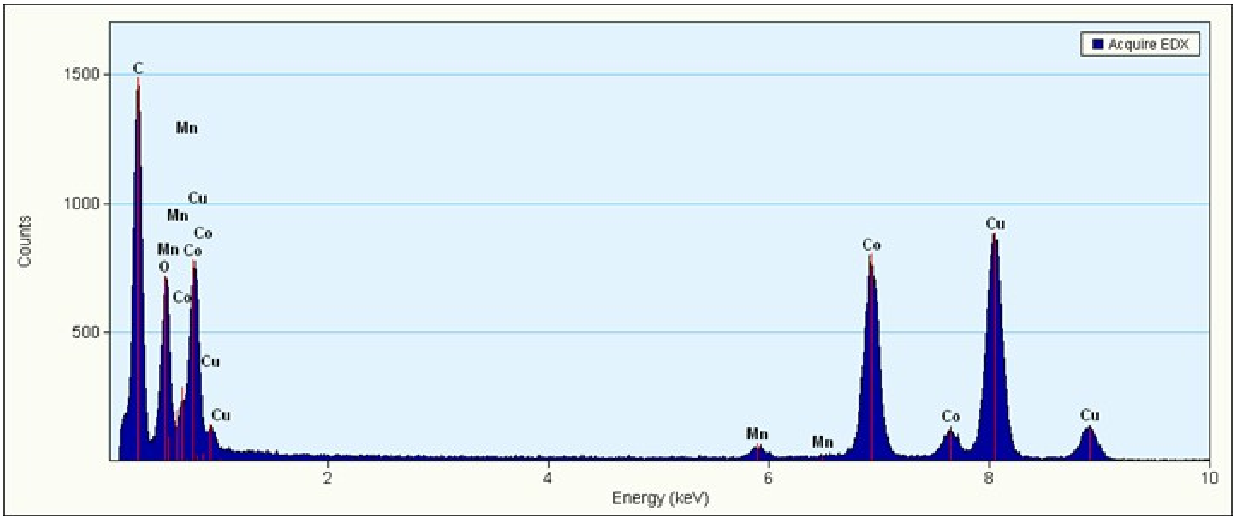

Fig. S3. The presence of manganese and cobalt in the cobalt oxalate precursor was determined by the EDX. Appearance of peaks for carbon and copper are due to TEM grid (carbon film on 300 mesh Cu-grid).

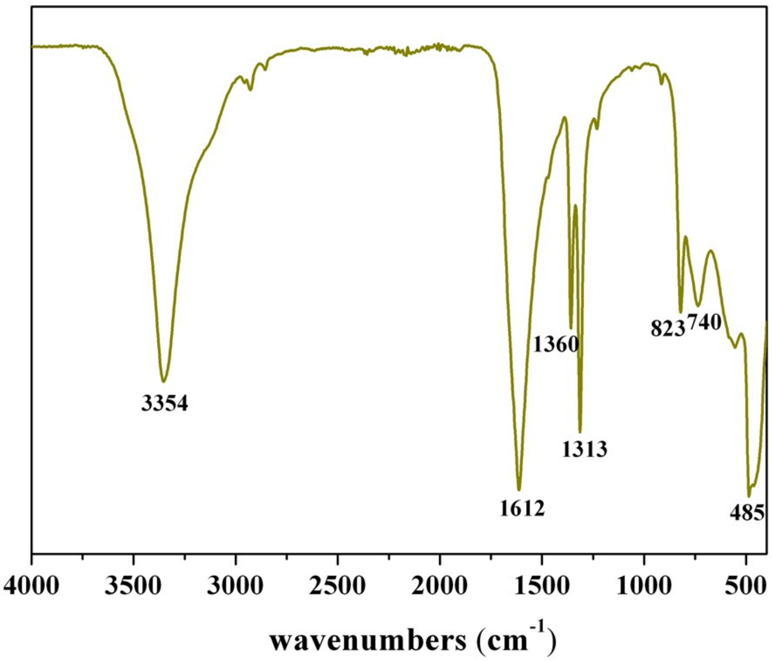

Fig. S4. FT-IR transmission spectrum of as-prepared manganese cobalt oxalate dihydrate precursor. The detailed description of IR absorption maxima is given in Table S3.[2,3]

Table S3. IR absorption maxima (cm^{-1}) of $Mn_{0.1}Co_{0.9}C_2O_4·2H_2O$ corresponding to Fig. S6. The values obtained here match well with literature reported metal oxalate precursor values.[2,3]

IR maxima / cm^{-1}	Assignments	IR maxima / cm^{-1}	Assignments
3354	$\gamma(OH)(H_2O)$	823	$\gamma_s(C–C) + \delta(OCO)$
1612	$\gamma_{as}(C–O)$	740	$\rho(H_2O)$
1360	$\gamma_s(C–O)$	485	δ ring
1313	$\delta(OCO)$		

as: asymetric, s:symmetric, γ:stretching, δ: bending, ρ:scissoring

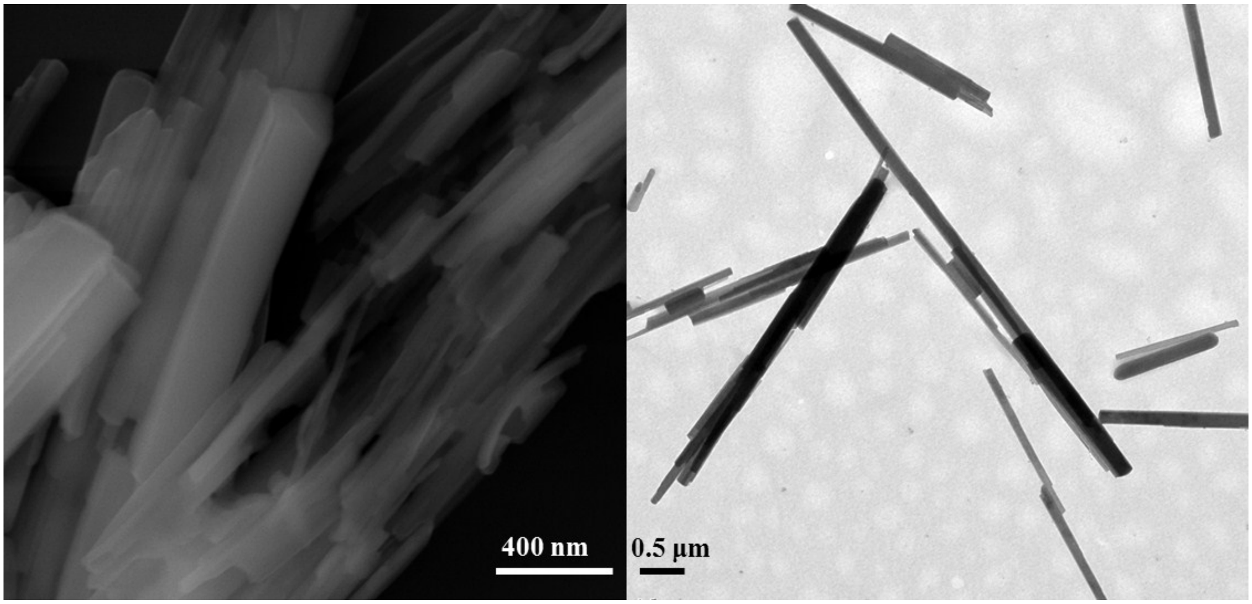

Fig. S5. The SEM (left) and TEM (right) images of $Mn_{0.1}Co_{0.9}C_2O_4{\cdot}2H_2O$ precursor. Both SEM and TEM revealed that oxalate precursor have nanorod morphology with a mean diameter of ~ 250-300 nm and length of several hundreds of nanometer. The BET surface area obtained was ~ 8 m^2/g.

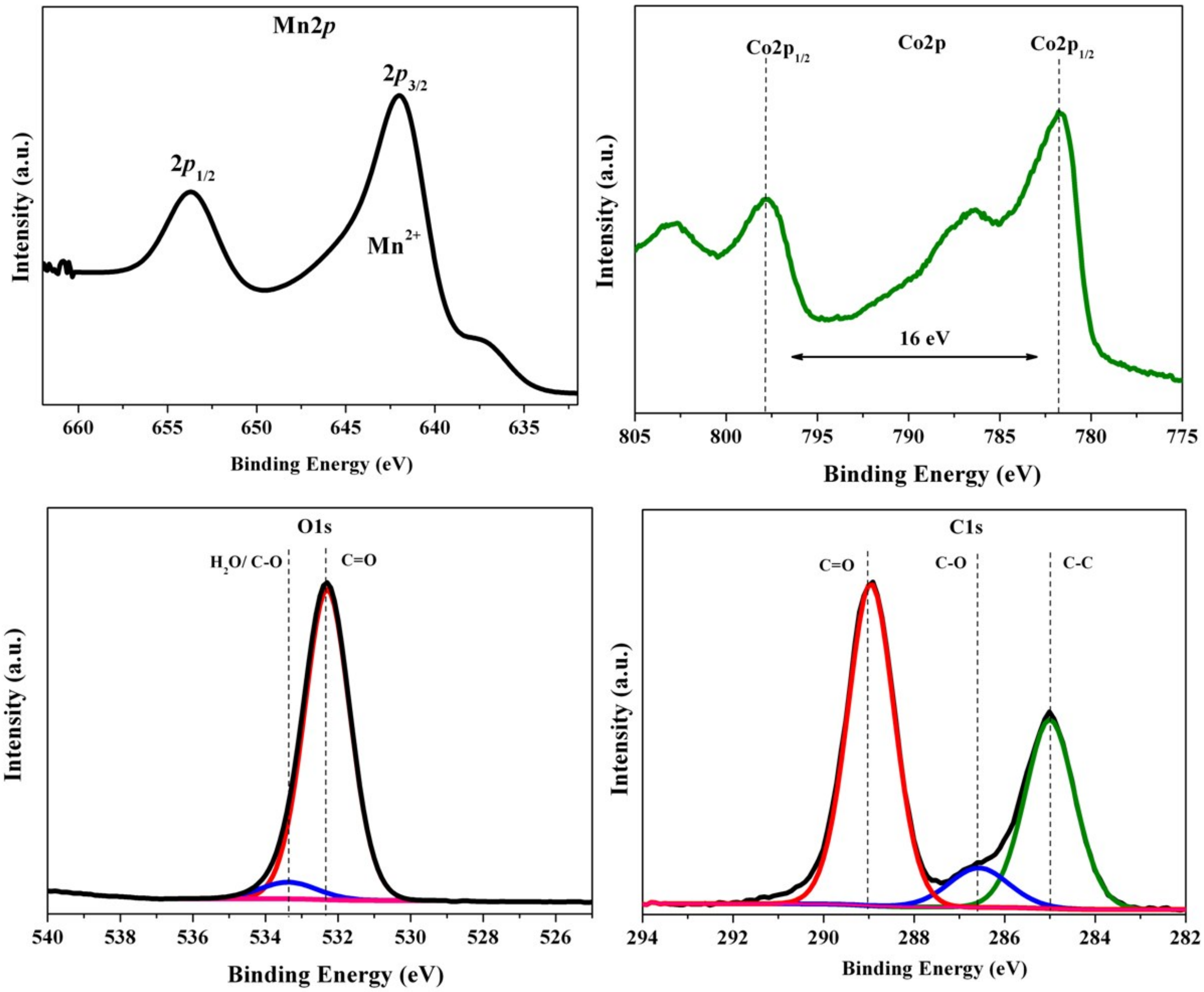

Fig. S6. High-resolution XPS spectra of the regions containing the Mn2p, Co2p, O1s, and C1s of $Mn_{0.1}Co_{0.9}C_2O_4{\cdot}2H_2O$. The Mn2p have binding energies (BE) at 641.9 eV for $Mn2p_{3/2}$ and 653.6 for $Mn2p_{1/2}$ which are similar to literature reported Mn(II).[4,5] The Co(II) and Co(III) have similar 2p BE but are often differentiated by the $Co2p_{1/2}$−$2p_{3/2}$ spin−orbit level energy spacing where the BE of 16 eV has been assigned to Co(II) and 15 eV to Co(III).[6] The BE's of cobalt here were found to be 797.7 eV for $Co2p_{1/2}$ and 781.7 for $Co2p_{3/2}$ with the difference of 16 eV and are consistent with Co(II).[6,7] The O1s BE peaks can be deconvoluted into two different carbon-oxygen functional groups. The peak at 533.3 eV corresponds to the BE of C–O bond or water and, the peak at 532.3 eV could be assigned to the C=O bond. The deconvoluted C 1*s* spectrum contains three BE peaks at 284.9 eV, 286.6 eV and 288.9 eV. The peaks at 284.9 eV and 286.6 eV are attributed to the carbon in C–C and C–O environments whereas the peak at 288.8 eV could be attributed to the C=O from the oxalate anion.[8,9]

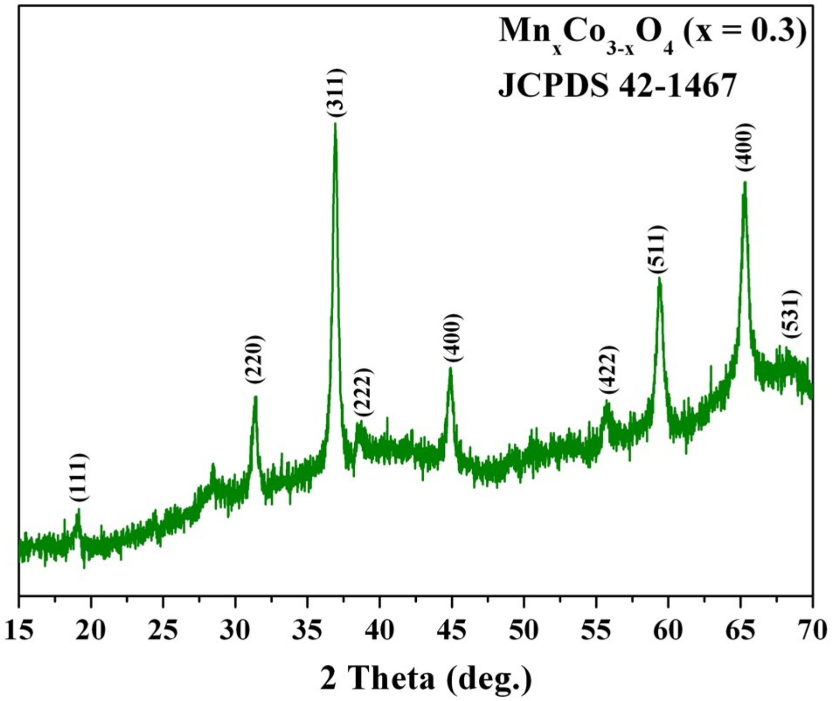

Fig. S7. PXRD pattern and Miller indices (hkl) of MCO, $Mn_{0.3}Co_{2.7}O_4$, (JCPDS 42-1467). The pattern was also slightly shifted in comparison to pure cobalt oxide because of the presence of Mn in the crystal lattice of the spinel structure. The amount of manganese and cobalt present in the oxide was determined by EDX and ICP-AES analysis.

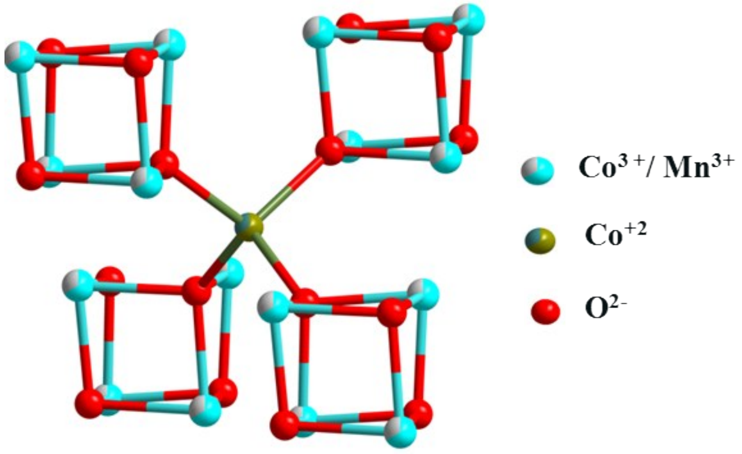

Fig. S8. The crystal structure of $Mn_{0.3}Co_{2.7}O_4$which crystallizes in the normal spinel (AB_2O_4; A = divalent and B = trivalent metal) structure with Co^{2+} atoms in tetrahedral and Co^{3+} atoms in the octahedral sites.[10] From XPS it was clear that the oxidation state of Mn is +3 and therefore, it is reasonable to assume that Mn^{3+} atoms are substituted in the crystal sites of Co^{3+} (octahedral position).[11]

Table S4. Quantification of manganese and cobalt ratio in $Mn_{0.3}Co_{2.7}O_4$ (MCO) was obtained by EDX and ICP-AES. Three independent measurements were performed for the reliability of the experiments.

	Mn:Co (EDX)	Mn:Co (ICP-AES)
MCO	0.28:2.72	0.29:2.71
	0.29:2.73	0.3:2.7
		0.3:2.7
Averaged	**0.285/2.725**	**0.3:2.7**

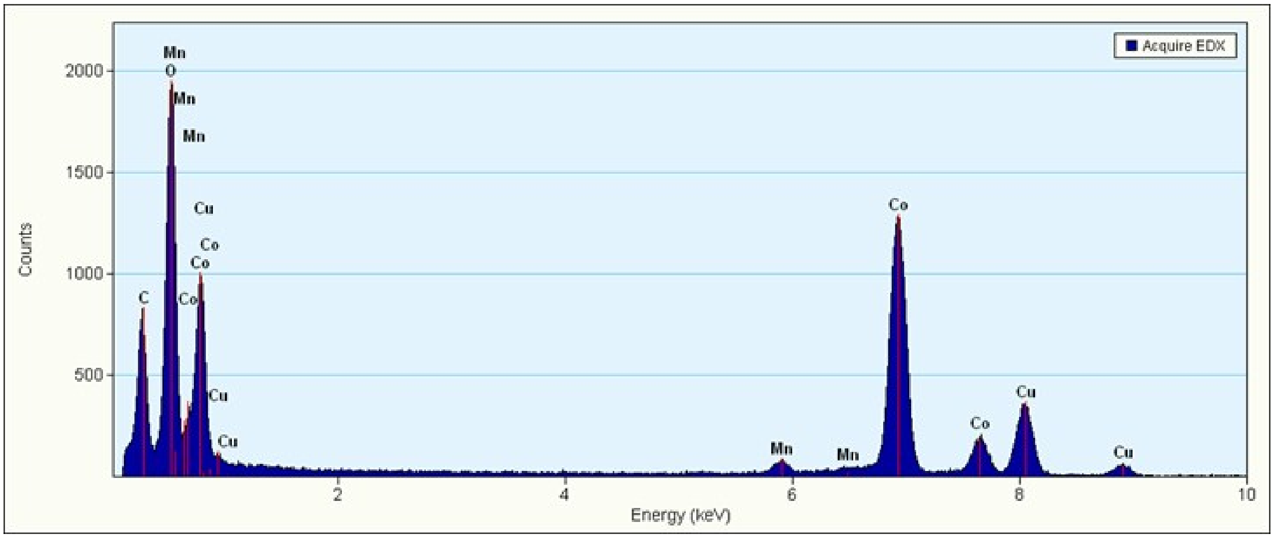

Fig. S9. The presence of manganese and cobalt in MCO was determined by the EDX. Appearance of peaks for carbon and copper are due to TEM grid (carbon film on 300 mesh Cu-grid).

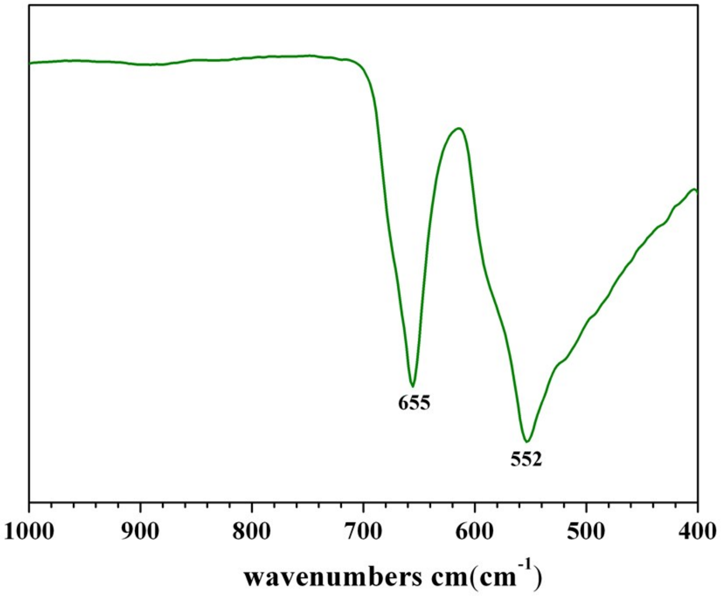

Fig. S10. FT-IR transmission spectrum of MCO in the region 400-1000 cm^{-1} showing symmetric Co—O / Mn—O stretching vibrations. The depicted spectrum is in accordance with the literature reported spectra of cobalt and manganese oxides.[3]

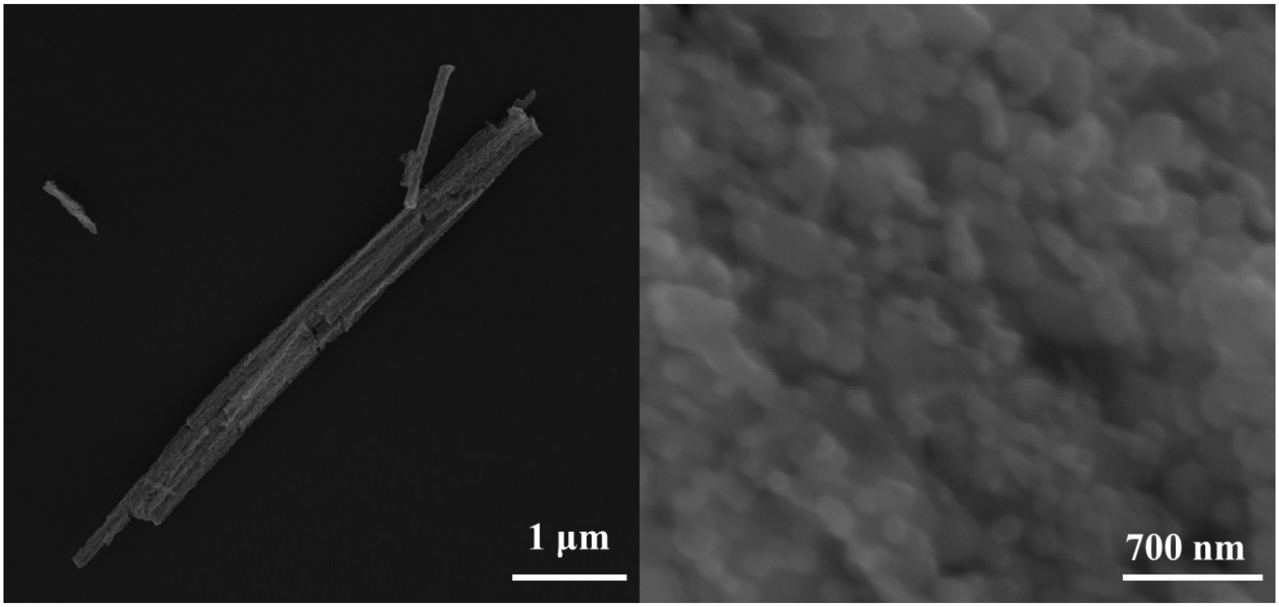

Fig. S11. The SEM (left) and high resolution SEM (right) micrographs of MCO showing rod-type morphology consisting of very small nanoparticles.

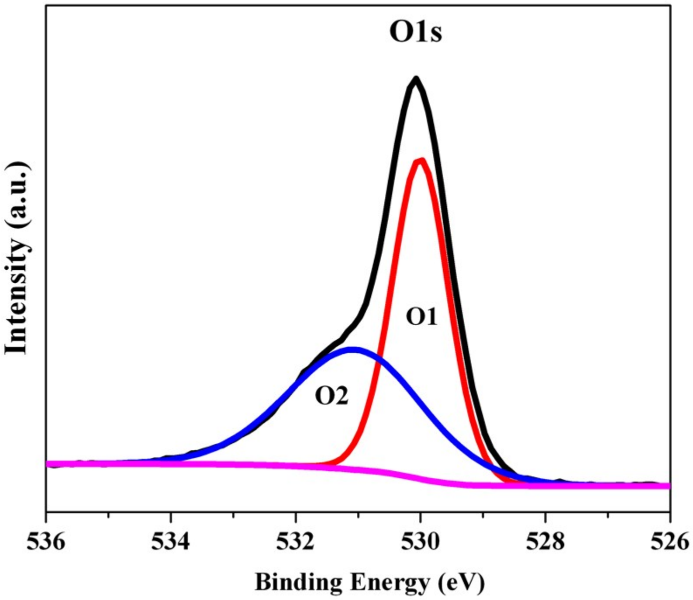

Fig. S12. The O1s XPS spectrum of MCO. The O1s spectrum could be deconvoluted into O1 and O2 peaks. The O1 peak at ~ 530 eV corresponds to metal–oxygen bonds of metal oxide whereas O2 at ~ 531.2 eV was assigned to oxygen in –OH groups, indicating the surface of the material is hydroxylated due to the consequence of either surface hydroxides or substitution of oxygen atoms at the surface by hydroxyl groups.[12-15]

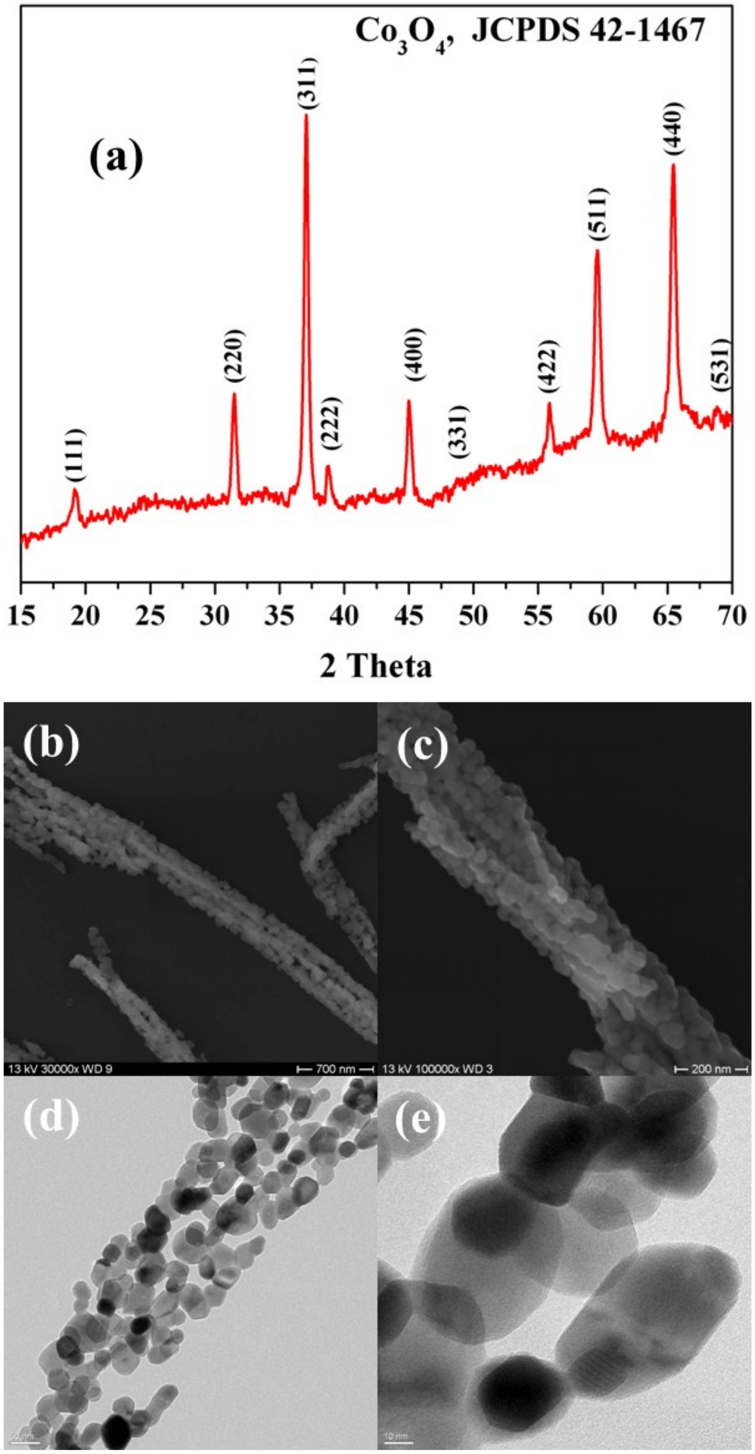

Fig. S13. (a) The PXRD of Co_3O_4 synthesized by a similar method (treating $CoC_2O_4{\cdot}2H_2O$ in air at 400 ˚C) without the presence of Mn.[7] The SEM (b), HRSEM (c), TEM (d) and HRTEM (e) image showed that the morphology of Co_3O_4 was similar to $Mn_{0.3}Co_{2.7}O_4$ and comprises of nanochains. The BET area of Co_3O_4 was about 12 m^2/g.

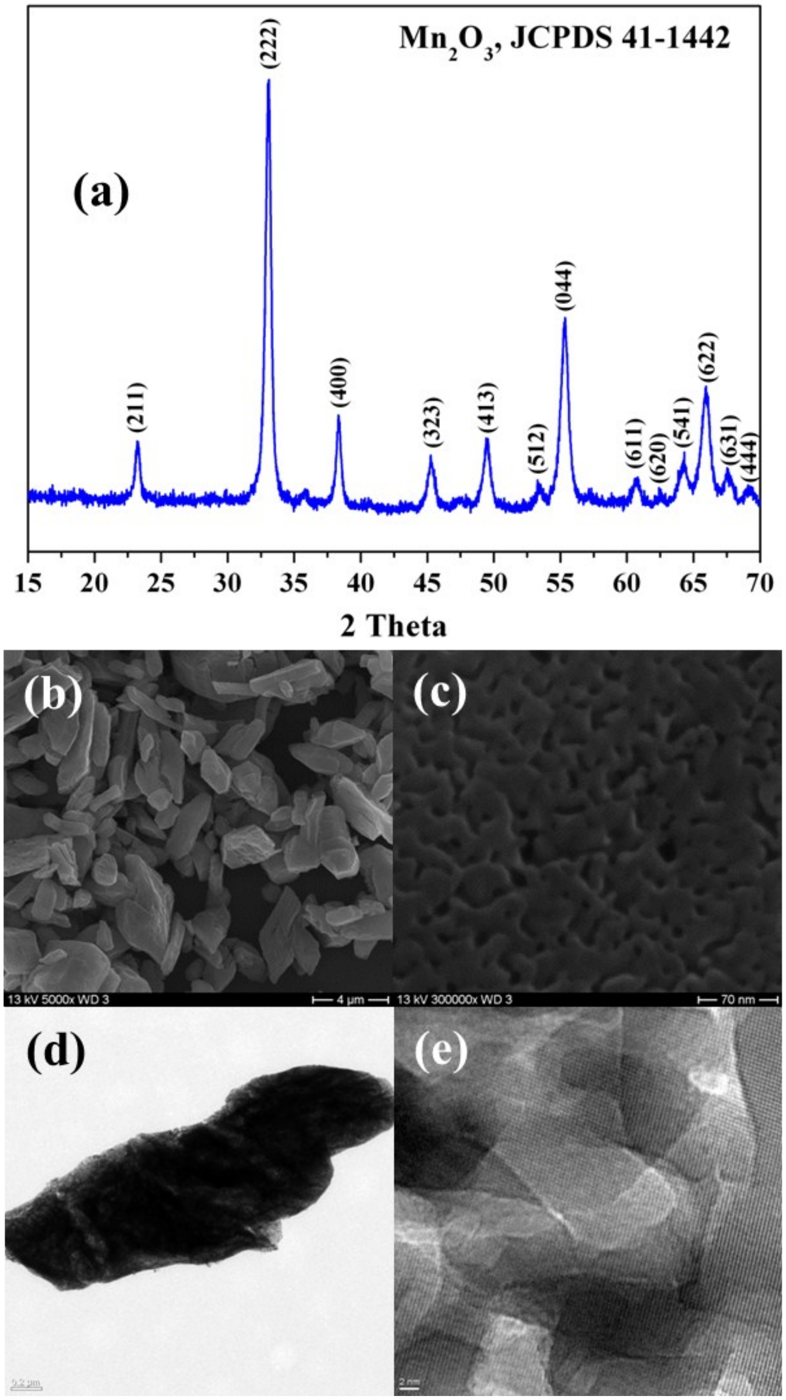

Fig. S14. (a) The PXRD of Mn_2O_3 synthesized by a similar method (treating $MnC_2O_4{\cdot}2H_2O$ in air at 400 ˚C) without the presence of Co.[16] The SEM (b), HRSEM (c), TEM (d) and HRTEM (e) image showed that the morphology of Mn_2O_3 was very different forming porous net type structures. The BET area of Mn_2O_3 was ~ 49 m^2/g.

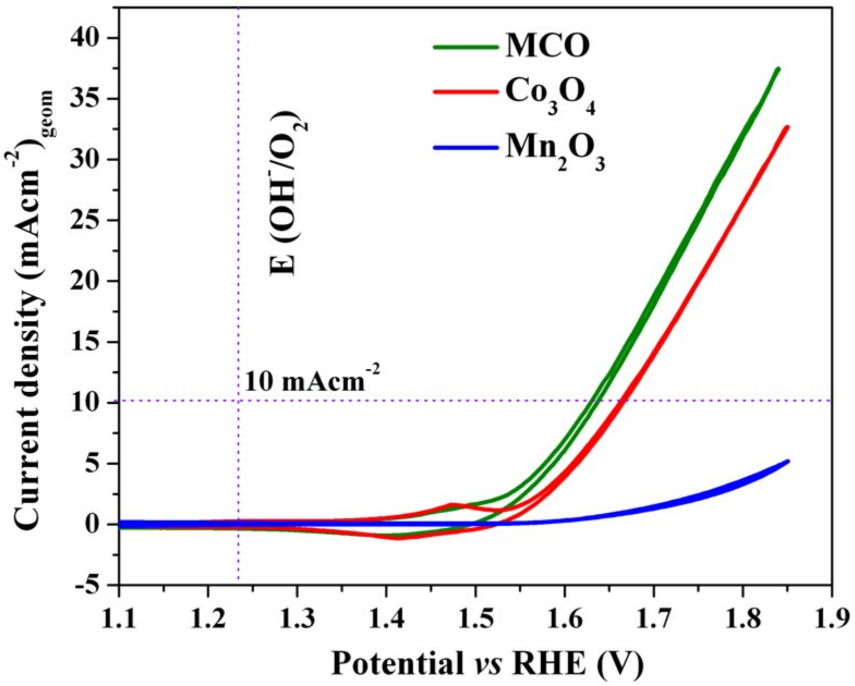

Fig. S15. Cyclic voltammetry (CV) of MCO versus Co_3O_4 and Mn_2O_3 in 0.1 M KOH solution with a scan rate of 20 mV/s on FTO substrates (loading ~ 1 mg).

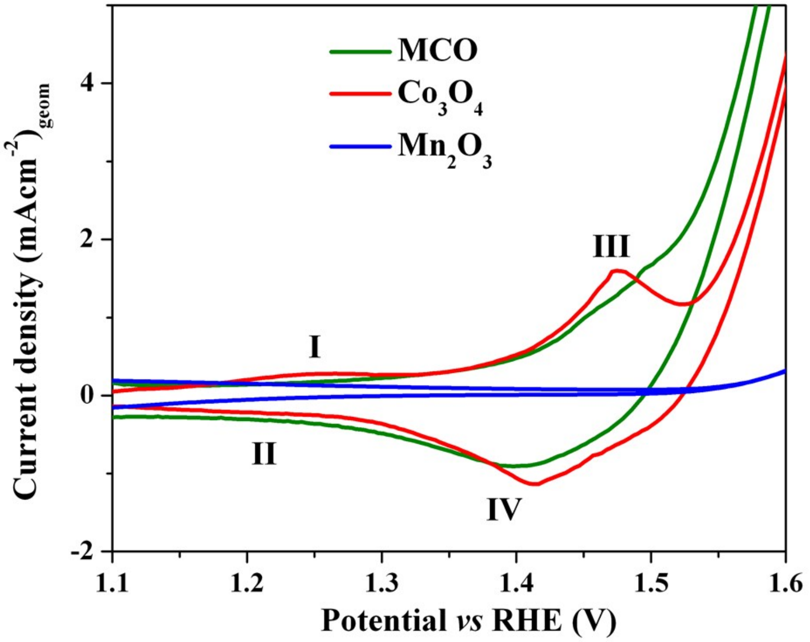

Fig. S16. Cyclic voltammograms of MCO versus Co_3O_4, Mn_2O_3 electrodes recorded at a potential sweep rate of 20 mV/s in 0.1 M KOH solution.[17-20]

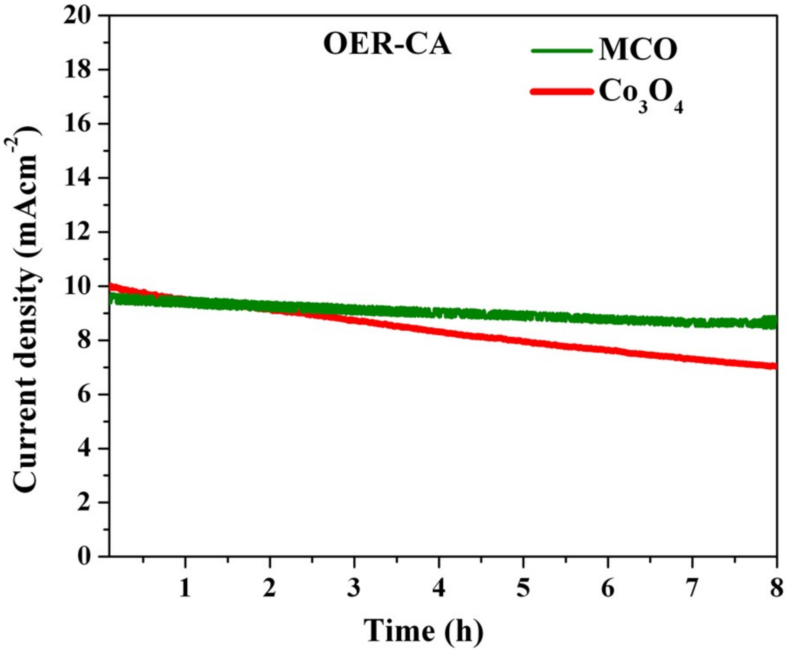

Fig. S17. Current-time chronoamperometry responses of MCO and Co_3O_4 measured at 1.62 V and 1.66 V vs RHE in 0.1 M KOH solution. The current was almost stable for MCO, however, in the case of Co_3O_4, about 30% initial activity was lost over the period of 8h.

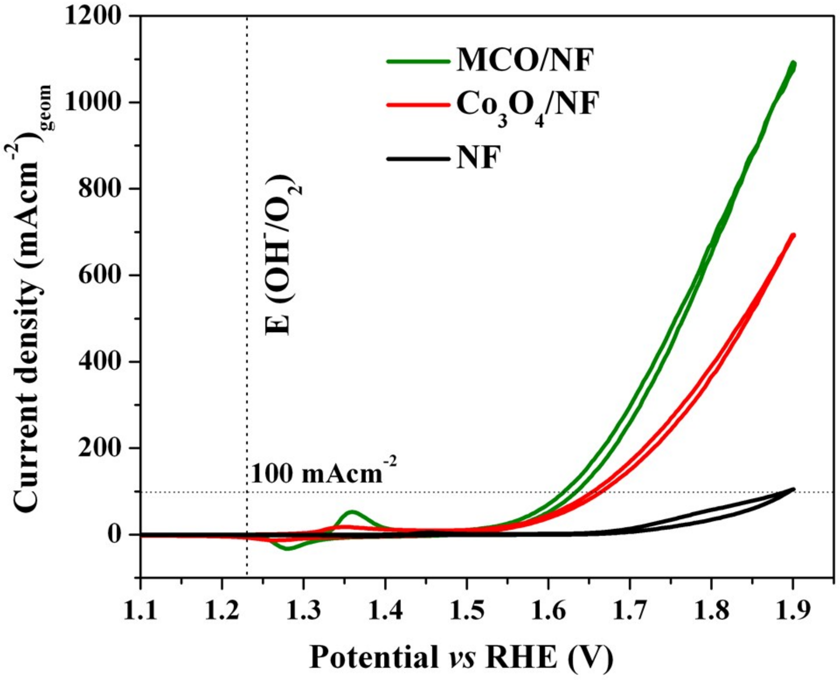

Fig. S18. Cyclic voltammetry (CV) of MCO, Co_3O_4 and Mn_2O_3 in 1 M KOH solution with a scan rate of 20 mV/s on NF substrates (loading ~ 3 mg).

Table S5. The comparison of OER overpotentials of MCO with other superior selected non-noble catalysts 1 M KOH (pH 14).

Catalyst	Current density (mAcm^{-2})	Overpotential (mV)	Reference
MCO	**10**	**320**	**This work**
Co_3O_4	**10**	**360**	**This work**
Mn_2O_3	**10**	**560**	**This work**
RuO_2	**10**	**350**	**This work**
IrO_2	**10**	**410**	**This work**
Pt	**10**	**650**	**This work**
Co-P/Cu	10	345	[21]
NiCo/NS	10	334	[22]
NiCo LDH	10	367	[23]
$Ni_xCo_{3-x}O_4$ NWs/Ti	10	370	[24]
$Ni_{1-x}Fe_x$ NC/GC	10	330	[25]
Co_3O_4/ $NiCo_2O_4$ DSNCs	10	340	[26]
CoP/Cu	10	345	[21]
CoCo LDH	10	393	[22]
N-G/CoO	10	340	[27]
Co_3O_4/N-rmGO	10	320	[28]
$CoFeO_x$	10	360	[29]
$NiFeO_x$	10	350	[29]
MnO_x	10	573	[30]
MoO_2/NF	10	250	[31]
MoO_2/NF compact	10	500	[31]
Ni_2P/FTO	10	400	[32]
Ni_2P/FTO	10	500	[32]
Ni_xP_y-325	10	320	[33]
Ni-P film	10	344	[34]
Co_3O_4@CoO SC	10	430	[35]
FeNi oxide	10	380	[36]
$CoSe_2$	10	320	[37]
CoMn LDH	10	324	[38]
Co_3O_4-MTA	10	400	[39]
$CoTe_2$	10	380	[40]
Co- Birnessite	10	360	[41]
Co_3ZnC	10	366	[42]
$Co(OH)_2$	10	325	[43]
CoO_x	10	325	[44]
CoO	10	497	[45]
Co_3O_4	10	497	[45]
Co	10	537	[45]
CoO_x electrodeposited	10	380	[46]

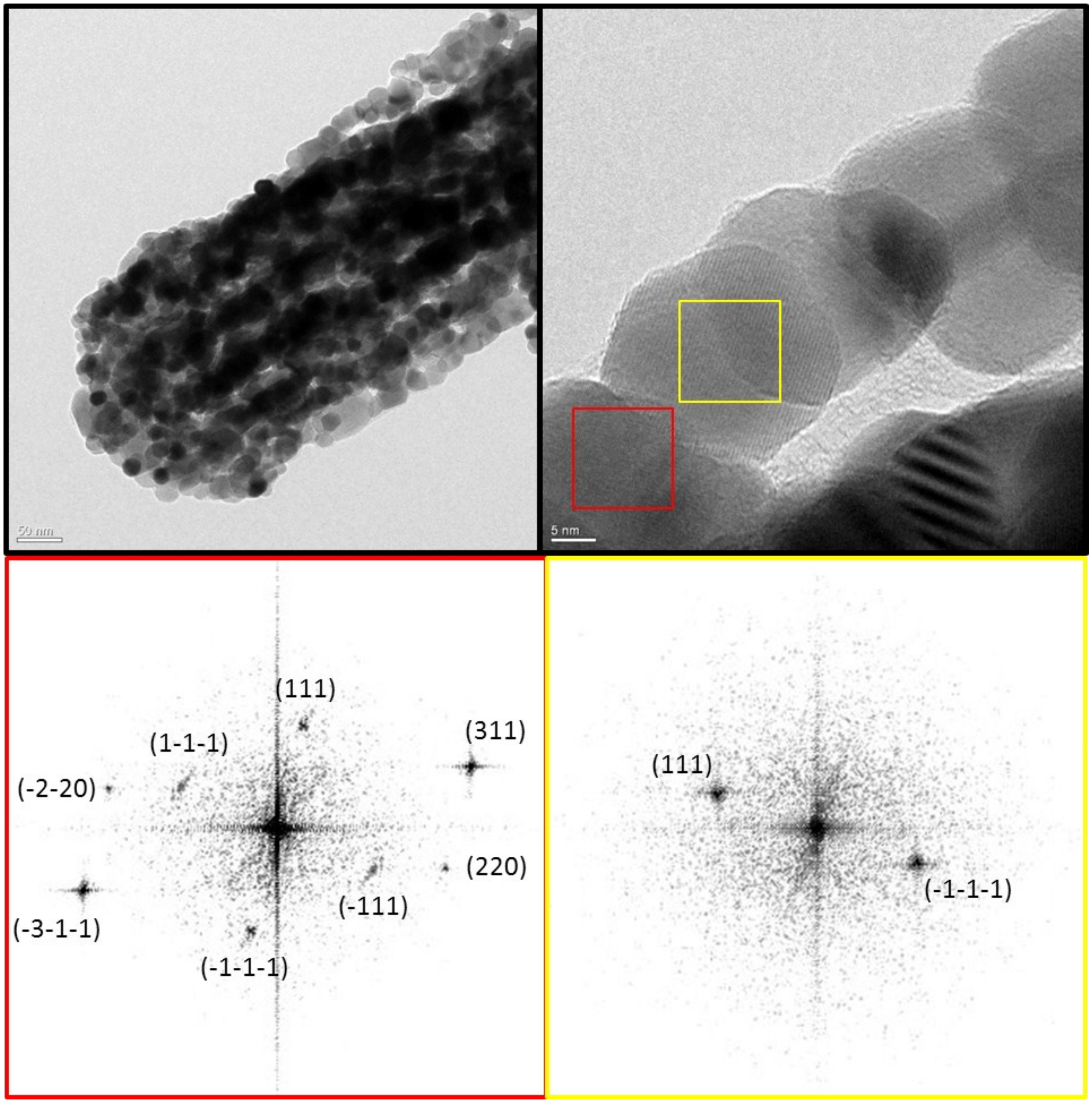

Fig. S19. The TEM (scale bar 50 nm), HRTEM (5 nm) images and their corresponding SAED patterns of as prepared MCO on FTO. No amorphous shell was seen on the surface of catalyst confirming the phase purity of the product.

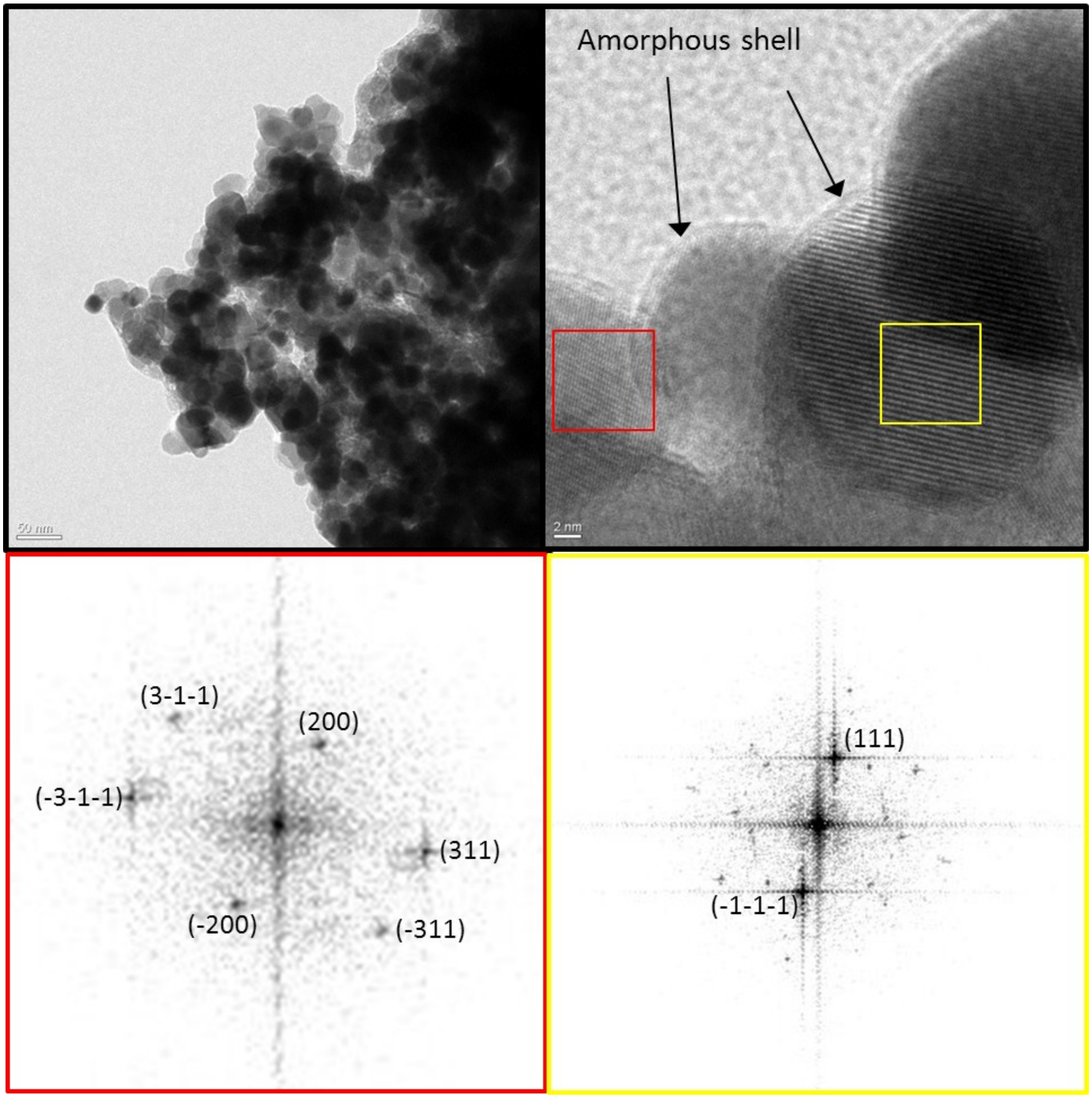

Fig. S20. The TEM (scale bar 50 nm), HRTEM (2 nm) images and their corresponding SAED patterns of MCO after the chronoamperometric measurements at an applied potential of 1.53 V vs RHE for 8 h in 0.1 M KOH. A thin amorphous shell was resulted on the surface of catalyst.

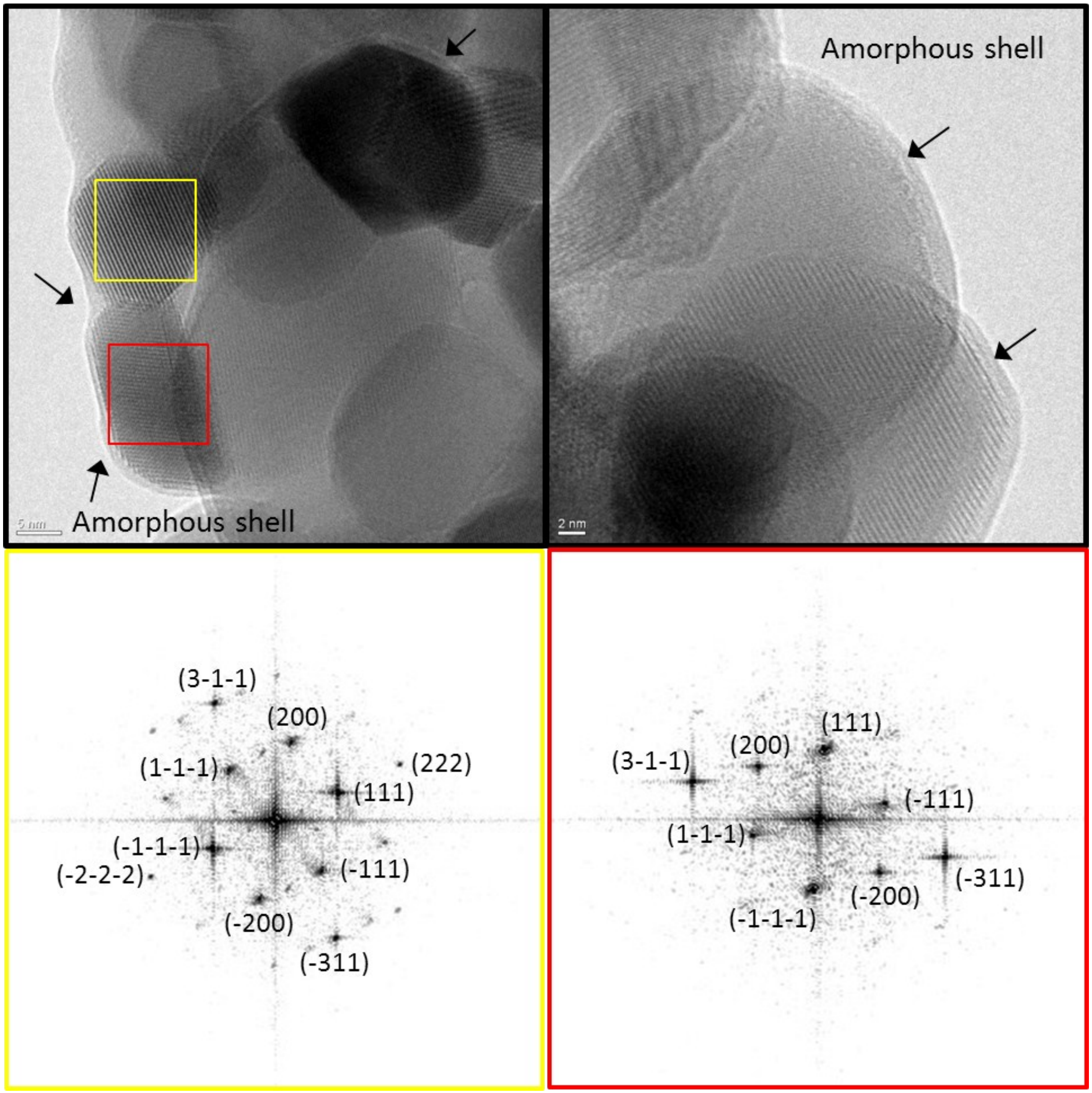

Fig. S21. The TEM (scale bar 5 nm), HRTEM (2 nm) images and their corresponding SAED patterns of MCO after the chronoamperometric measurements at a potential of 1.62 V vs RHE for 8 h in 0.1 M KOH. The thickness of amorphous shell was clearly increased on the surface of the catalyst.

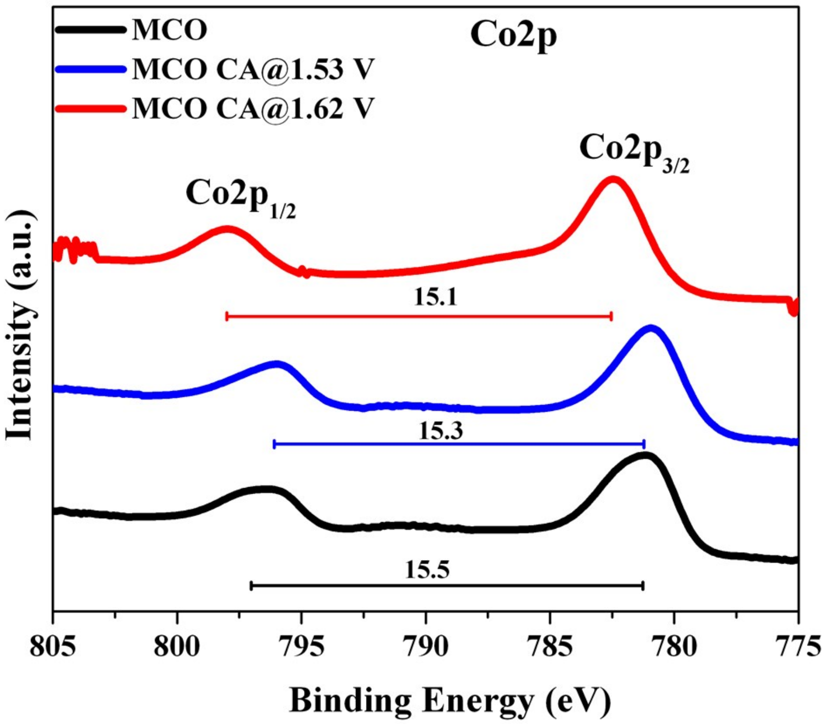

Fig. S22. The Co2p XPS spectra of MCO at the onset and elevated oxygen evolution electrode potential. The Co(II) and Co(III) have similar 2p BE but are often differentiated by the Co2p$_{1/2}$−2p$_{3/2}$ spin−orbit level energy spacing while the BE of 16 eV can be assigned to Co(II) and 15 eV to Co(III). In the XPS study, Co2p spectra displayed a spin−orbit level energy spacing of 15.3 eV after applying an onset potential in comparison to the as-synthesised MCO with spacing 15.5 eV. This directly indicates that there is an increase in the amount of Co(III) and probably in the surface structure at the onset potential. However, at an applied potential 1.62 V, a large amount of Co(III) was detected (spin−orbit level energy spacing 15.1 eV) from the higher energy shift of the peak that evidences major changes in the near-surface region.[44,47-49]

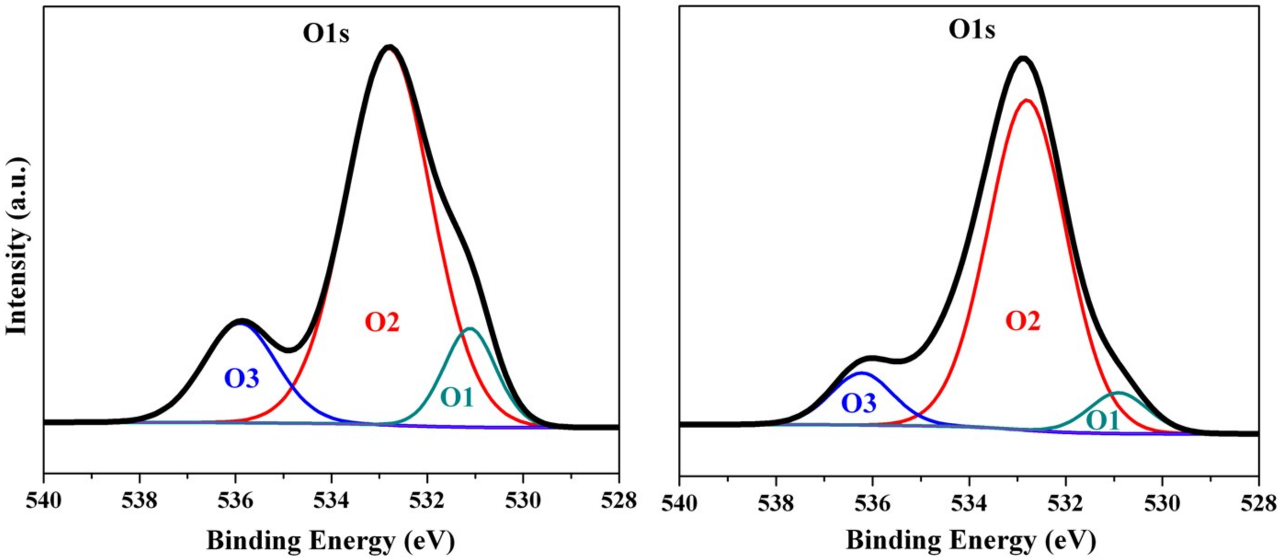

Fig. S23. The O1s XPS spectra of (left) $Mn_{0.3}Co_{2.7}O_4$ (MCO) at an applied potential of 1.53 V (right) 1.62 V vs RHE after the current-time chronoamperometry for 8 h. The O1s spectrum in both cases was deconvoluted into three peaks (O1, O2 and O3). The peaks (O1) at ~ 530.5 eV correspond to metal–oxygen bonds in metal oxides. The peaks (O2) between ~ 530.8 to 535.5 eV were largely increased in comparison to the as synthesized MCO before electrochemical water oxidation with higher fraction of –OH groups confirming, the surface of the material is hydroxylated. The peaks (O3) at around ~ 536 can be correlated to the absorbed water molecules on the surface of the materials. The values obtained here are in accordance with the other literature reported oxide materials.[44,47-49]

References

1. R. Deyrieux, C. Berro and A. Peneloux, *Bull. Soc. Chim. Fr.*, 1973, 25-34.
2. D. Wang, Q. Wang and T. Wang, *Inorg. Chem.*, 2011, **50**, 6482-6492.
3. M. Salavati-Niasari, N. Mir and F. Davar, *J. Phys. Chem. Solids*, 2009, **70**, 847-852.
4. H. W. Nesbitt and D. Banerjee, *Am. Mineral.*, 1998, **83**, 305-315.
5. P. W. Menezes, A. Indra, O. Levy, K. Kailasam, V. Gutkin, J. Pfrommer and M. Driess, *Chem. Commun.*, 2015, **51**, 5005-5008.
6. M. Oku and K. Hirokawa, *J. Electron Spectros. Relat. Phenom.*, 1976, **8**, 475-481.
7. P. W. Menezes, A. Indra, D. Gonzalez-Flores, N. R. Sahraie, I. Zaharieva, M. Schwarze, P. Strasser, H. Dau and M. Driess, *ACS Catal.*, 2015, **5**, 2017-2027.
8. V. Shinde, A. B. Mandale, K. R. Patil, A. B. Gaikwad and P. P. Patil, *Surf. Coat. Technology*, 2006, **200**, 5094-5101.
9. X. Yuan, M. Zhang, X. Chen, N. An, G. Liu, Y. Liu, W. Zhang, W. Yan and M. Jia, *Appl.Catal. A*, 2012, **439**, 149-155.
10. W. L. Roth, *J. Phys. Chem. Solids*, 1964, **25**, 1-10.
11. C. Li, X. P. Han, F. Y. Cheng, Y. X. Hu, C. C. Chen and J. Chen, *Nat. Commun.*, 2015, **6**, 7345.

12. M. Prabu, K. Ketpang and S. Shanmugam, *Nanoscale*, **6**, 3173-3181.
13. Z.-Y. Tian, P. H. T. Ngamou, V. Vannier, K. Kohse-Hoeinghaus and N. Bahlawane, *Appl. Catal. B*, **117**, 125-134.
14. B. J. Tan, K. J. Klabunde and P. M. A. Sherwood, *J. Am. Chem. Soc.*, 1991, **113**, 855-861.
15. S. Ma, L. Sun, L. Cong, X. Gao, C. Yao, X. Guo, L. Tai, P. Mei, Y. Zeng, H. Xie and R. Wang, *J. Phys. Chem. C*, 2013, **117**, 25890-25897.
16. P. W. Menezes, A. Indra, P. Littlewood, M. Schwarze, C. Göbel, R. Schomäcker and M. Driess, *ChemSusChem*, 2014, **7**, 2202-2211.
17. X. Liu, Z. Chang, L. Luo, T. Xu, X. Lei, J. Liu and X. Sun, *Chem. Mater.*, 2014, **26**, 1889-1895.
18. G. Spinolo, S. Ardizzone and S. Trasatti, *J. Electroanal. Chem.*, 1997, **423**, 49-57.
19. S. Palmas, F. Ferrara, A. Vacca, M. Mascia and A. M. Polcaro, *Electrochim. Acta*, 2007, **53**, 400-406.
20. E. B. Castro and C. A. Gervasi, *Int. J. Hydrogen Energy*, 2000, **25**, 1163-1170.
21. N. Jiang, B. You, M. L. Sheng and Y. J. Sun, *Angew. Chem. Int. Ed.*, 2015, **54**, 6251-6254.
22. F. Song and X. L. Hu, *Nat. Chem.*, 2014, **5**, 4477.
23. H. F. Liang, F. Meng, M. Caban-Acevedo, L. S. Li, A. Forticaux, L. C. Xiu, Z. C. Wang and S. Jin, *Nano Lett.*, 2015, **15**, 1421-1427.
24. Y. G. Li, P. Hasin and Y. Y. Wu, *Adv. Mater.*, 2010, **22**, 1926-1929.
25. X. Zhang, H. M. Xu, X. X. Li, Y. Y. Li, T. B. Yang and Y. Y. Liang, *ACS Catal.*, 2016, **6**, 580-588.
26. H. Hu, B. Y. Guan, B. Y. Xia and X. W. Lou, *J. Am. Chem. Soc.* , 2015, **137**, 5590-5595.
27. S. Mao, Z. H. Wen, T. Z. Huang, Y. Hou and J. H. Chen, *Energy Environ. Sci.*, 2014, **7**, 609-616.
28. Y. Liang, Y. Li, H. Wang, J. Zhou, J. Wang, T. Regier and H. Dai, *Nat. Mater.*, 2011, **10**, 780-786.
29. C. C. L. McCrory, S. Jung, J. C. Peters and T. F. Jaramillo, *J. Am. Chem. Soc.*, 2014, **135**, 16977-16987.
30. L. Trotochaud, J. K. Ranney, K. N. Williams and S. W. Boettcher, *J. Am. Chem. Soc.*, 2012, **134**, 17253-17261.
31. Y. S. Jin, H. T. Wang, J. J. Li, X. Yue, Y. J. Han, P. K. Shen and Y. Cui, *Adv. Mater.*, 2016, **28**, 3785-3790.
32. A. Han, H. L. Chen, Z. J. Sun, J. Xu and P. W. Du, *Chem. Commun.*, 2015, **51**, 11626-11629.
33. J. Y. Li, J. Li, X. M. Zhou, Z. M. Xia, W. Gao, Y. Y. Ma and Y. Q. Qu, *ACS Appl. Mater. Inter.*, 2016, **8**, 10826-10834.
34. N. Jiang, B. You, M. L. Sheng and Y. J. Sun, *ChemCatChem*, 2016, **8**, 106-112.
35. C. W. Tung, Y. Y. Hsu, Y. P. Shen, Y. X. Zheng, T. S. Chan, H. S. Sheu, Y. C. Cheng and H. M. Chen, *Nat. Chem.*, 2015, **6**, 8106.
36. J. Landon, E. Demeter, N. Inoglu, C. Keturakis, I. E. Wachs, R. Vasic, A. I. Frenkel and J. R. Kitchin, *ACS Catal.*, 2012, **2**, 1793-1801.
37. Y. W. Liu, H. Cheng, M. J. Lyu, S. J. Fan, Q. H. Liu, W. S. Zhang, Y. D. Zhi, C. M. Wang, C. Xiao, S. Q. Wei, B. J. Ye and Y. Xie, *J. Am. Chem. Soc.*, 2014, **136**, 15670-15675.

38. F. Song and X. L. Hu, *J. Am. Chem. Soc.*, 2014, **136**, 16481-16484.
39. Y. P. Zhu, T. Y. Ma, M. Jaroniec and S. Z. Qiao, *Angew. Chem. Int. Ed.*, 2017, **56**, 1324-1328.
40. I. G. McKendry, A. C. Thenuwara, J. W. Sun, H. W. Peng, J. P. Perdew, D. R. Strongin and M. J. Zdilla, *ACS Catal.*, 2016, **6**, 7393-7397.
41. A. C. Thenuwara, S. L. Shumlas, N. H. Attanayake, Y. V. Aulin, I. G. McKendry, Q. Qiao, Y. M. Zhu, E. Borguet, M. J. Zdilla and D. R. Strongin, *ACS Catal.*, 2016, **6**, 7739-7743.
42. J. W. Su, G. L. Xia, R. Li, Y. Yang, J. T. Chen, R. H. Shi, P. Jiang and Q. W. Chen, *J. Mater. Chem. A*, 2016, **4**, 9204-9212.
43. P. F. Liu, S. Yang, L. R. Zheng, B. Zhang and H. G. Yang, *J. Mater. Chem. A*, 2016, **4**, 9578-9584.
44. A. Indra, P. W. Menezes, C. Das, C. Gobel, M. Tallarida, D. Schmeisser and M. Driess, *J. Mater. Chem. A*, 2017, **5**, 5171-5177.
45. N. H. Chou, P. N. Ross, A. T. Bell and T. D. Tilley, *ChemSusChem*, 2011, 4, 1566-1569.
46. M. D. Merrill and R. C. Dougherty, *J. Phy. Chem. C*, 2008, **112**, 3655-3666.
47. P. W. Menezes, A. Indra, C. Das, C. Walter, C. Göbel, V. Gutkin, D. Schmeisser and M. Driess, *ACS Catal.*, 2017, **7**, 103-109.
48. J. Pfrommer, A. Azarpira, A. Steigert, K. Olech, P. W. Menezes, R. F. Duarte, X. X. Liao, R. G. Wilks, M. Bar, T. Schedel-Niedrig and M. Driess, *ChemCatChem*, 2017, **9**, 672-676.
49. P. W. Menezes, A. Indra, A. Bergmann, P. Chernev, C. Walter, H. Dau, P. Strasser and M. Driess, *J. Mater. Chem. A*, 2016, **4**, 10014-10022.